Yu *et al. Cellular & Molecular Biology Letters* (2025) 30:58
https://doi.org/10.1186/s11658-025-00737-3

Cellular & Molecular
Biology Letters

RESEARCH ARTICLE **Open Access**

Multi-omics integration reveals Vha68-3 as a testicular aging-specific factor that coordinates spermatid elongation through mitochondrial metabolic homeostasis

Jun Yu[1*†], Qiuru Huang[1†], Yangbo Fu[1†], Lei He[1], Cong Shen[2], Xia Chen[1,3], Zhiran Li[4], Jiaxin Li[1], Chenyu Wang[1], Xinda Wang[1], Binbin Yang[1], Ziwen Lin[1], Chen Qiao[5], Xiaofang Tan[6], Xiaoqing Yang[7], Hao Chen[8], Ying Zheng[9], Bo Zheng[2*] and Fei Sun[1,10*]

†Jun Yu, Qiuru Huang, Yangbo Fu, Lei He, and Cong Shen contributed equally.

*Correspondence:
yujun9117@126.com;
bozheng@njmu.edu.cn;
sunfei@ntu.edu.cn

[1] Institute of Reproductive Medicine, Medical School, Nantong University, Nantong 226001, China
[2] State Key Laboratory of Reproductive Medicine and Offspring Health, Center for Reproduction and Genetics, Suzhou Municipal Hospital, Gusu School, The Affiliated Suzhou Hospital of Nanjing Medical University, Nanjing Medical University, Suzhou 215002, China
Full list of author information is available at the end of the article

Abstract

Background: Testicular aging has profound effects on spermatogenesis, sperm function, and the spermatogenic microenvironment, contributing to reduced male fertility. However, the precise molecular mechanisms by which mitochondria influence spermiogenesis during aging still remain largely unclear.

Methods: Vha68-3 KO flies were generated using the CRISPR/Cas9 technique. Testicular phenotypes and functions were mainly observed through immunofluorescence staining and transmission electron microscopy. Multi-omics study was mainly conducted through single-cell RNA sequencing and transcriptome–metabolomics association analysis. Vha68-3 binding proteins were identified via liquid chromatography–tandem mass spectrometry. The therapeutic potential of modulating mitochondrial metabolism for testicular aging mainly relied on the dietary intake of related compounds in fruit flies.

Results: In this study, we identified Vha68-3, a testis-specific subunit of the V-type adenosine triphosphate (ATP) synthase, predominantly localized in the tails of elongated spermatids, as a key age-related regulator of male fertility and spermatid elongation in *Drosophila* testes. Crucially, *Vha68-3* deficiency impaired mitochondrial homeostasis in elongated spermatids during testicular aging. Through a multi-omics approach, including single-cell transcriptomics, protein interaction mapping of Vha68-3, and transcriptome–metabolome integration, we identified pyruvate metabolism as a critical pathway disrupted by *Vha68-3* deficiency. Moreover, dietary supplementation with pyruvate (PA), *S*-lactoylglutathione (SLG), and phosphoenolpyruvate (PEP) effectively alleviated mitochondrial dysfunction and testicular aging linked to *Vha68-3* deficiency.

Conclusions: Our findings uncover novel mechanisms by which mitochondrial metabolism regulates spermatid elongation and propose potential therapeutic strategies to combat mitochondrial metabolic disorders in aging testes.

Keywords: Spermiogenesis, Testicular aging, Mitochondrial homeostasis, Pyruvate metabolism, Multi-omics

Background

Spermiogenesis is an intricate and highly orchestrated biological process, characterized by the morphological transition from round to elongated spermatids. Disruptions during these transformations can result in structural abnormalities in spermatogenic cells, significantly affecting fertility [1]. Recently, researchers have focused on maintaining both structural integrity and functional balance throughout spermatid elongation [1–3]. Several genes have been identified as key regulators of the structural framework necessary for spermatid maturation and male fertility [4, 5]. Notably, genes such as centrosomal protein 78 (*CEP78*) and cilia and flagella associated protein 57 (*CFAP57*) play pivotal roles in flagella assembly [6, 7], while the RNA-binding protein FMR1 autosomal homolog 1 (FXR1), highly expressed in elongated spermatids, regulates stored mRNA activation through liquid–liquid phase separation, underscoring its critical role in spermatid maturation [8]. Furthermore, studies have confirmed that mutations in genes related to spermatid maturation, such as *FSIP2*, are central to the development of asthenozoospermia, with gene mutations leading to severe fibrous sheath disintegration, axonemal defects, and abnormal mitochondrial sheath structure [9–11]. These findings highlight the importance of morphological changes and structural elongation of spermatids in ensuring fertility.

In addition to spermatid morphology, spermiogenesis involves the elongation and structural modification of various organelles, including mitochondria, a key step in spermatogenesis [1]. During the early post-meiotic stage in *Drosophila* spermatids, mitochondria coalesce and merge to form two enlarged mitochondrial derivatives (referred to as major and minor), which subsequently elongate in parallel with the flagellar axoneme during the comet stage within the testis [12]. Despite recent advances, the regulatory mechanisms underlying mitochondrial damage-induced spermiogenesis disorders remain poorly understood. Classic model organisms, such as *Drosophila melanogaster*, have proven effective for studying spermiogenesis in testicular systems. A recent single-cell RNA sequencing (scRNA-seq) study in *Drosophila* testes identified mitochondrial dysfunction as a mediator of spermatid elongation defects, further implicating mitochondrial transport proteins in the maintenance of mitochondrial derivatives during spermatogenesis [13].

The V-type ATP synthase is widely conserved across species and primarily regulates intracellular transport, biosynthesis, pH homeostasis, and nutrient uptake [14, 15]. Its diverse functions are largely dictated by its subcellular localization [14, 15]. While prior studies have focused on its role in lysosomal acidification, recent evidence has extended its involvement to mitochondrial function and stress regulation, particularly through phosphorylation of activating transcription factor 4 (ATF4) via the mechanistic target of rapamycin complex 1 (mTORC1) [16]. Nevertheless, the direct regulation of mitochondrial homeostasis by V-type ATP synthase remains underexplored.

Testicular aging has profound effects on spermatogenesis, sperm function, and the spermatogenic microenvironment, contributing to reduced male fertility [17]. Although recent studies have shed light on the aging characteristics of mammalian and *Drosophila* testes [18, 19], the precise mechanisms by which mitochondria influence spermiogenesis during aging are still largely unknown. Furthermore, the role of the V-type ATPase 68 kDa subunit 3 (Vha68-3) in testicular function remains poorly characterized.

In this study, we demonstrate the role of Vha68-3 for spermiogenesis during testicular aging, where it predominantly localizes to the elongated spermatid tail in *Drosophila*. Our results suggest that Vha68-3 plays a crucial role in maintaining mitochondrial derivatives through mitochondrial metabolism, thereby promoting spermatid elongation and preserving male fertility during testicular aging. This discovery broadens our understanding of the V-type ATP synthase and its molecular targets, offering new insights into the mechanisms of mitochondrial damage-mediated spermiogenesis disorders, providing critical avenues for future research.

Methods

Generation of *Vha68-3* KO flies

Vha68-3 KO flies were generated using the CRISPR/Cas9 technique as previously described [20, 21]. Two guide RNAs (gRNAs) targeting the *Vha68-3* coding region were designed: sgRNA1 (5′-cccgcccgggaactactgcg-3′) and sgRNA2 (5′-acgtgggctgcggtgagcgc-3′). These purified gRNAs were combined and injected into nos-Cas9 embryos (Bloomington *Drosophila* Stock Center, #78782). Heterozygous mutants (F0 and F1) were identified through PCR and sequencing. The following primers were used: forward 5′-GGGTGATCCCGTCTACCAGA-3′, reverse 5′-CAGCCGAGCTCCCAAGTAAG-3′. Flies used for in vivo experiments were reared on standard cornmeal molasses agar medium at 25 °C with 40–60% relative humidity.

Phase-contrast microscopy

Phase-contrast microscopy was performed as previously described [22]. Briefly, testes were dissected in 1× phosphate-buffered saline (PBS), washed, and mounted on slides. The samples were coverslipped and examined using a phase-contrast microscope.

Stainings

Testes were dissected in 1× PBS, fixed in 4% paraformaldehyde (PFA) for 30 min, and washed three times with 0.3% PBS-Triton X-100 (PBST). Samples were blocked with 5% bovine serum albumin (BSA) for 30 min and then incubated with primary antibodies for 1 h at room temperature (RT). After three washes in 0.3% PBST, the samples were exposed to secondary antibodies for 1 h at RT in darkness. Following an additional three washes with PBST, the testes were stained with Hoechst-33342 (1.0 mg/ml, C0031, Solarbio) for 5 min before mounting. Primary antibodies included rabbit anti-Vha68-3 (Yu-Lab, 1:1000), mouse anti-Orb (4H8, DSHB, 1:50), mouse anti-Orb2 (4G8, DSHB, 1:50), rabbit anti-cleaved Caspase-3 (#9664, CST, 1:1000), mouse anti-ATP5A (ab14748, Abcam, 1:200), and rabbit anti-Tom20 (#42406, CST, 1:200). Secondary antibodies labeled with A488, Cy3, or A647 (Jackson ImmunoResearch Laboratories) were diluted to 1:800. Lysosomal compartments were stained with LysoTracker™ Red DND-99 (L7528, Thermo Fisher, 1:1000) according to the manufacturer's instructions.

TEM analysis

Testes were dissected and prepared for transmission electron microscopy (TEM) following a published protocol [23]. Samples were fixed in 2% glutaraldehyde at 4 ℃ overnight, washed, and post-fixed in 2% OsO4 in phosphate buffer at 4 ℃ for 2 h. After dehydration in graded ethanol concentrations, samples were embedded in Araldite resin. Ultrathin sections (60 nm) were cut, placed on copper grids, and stained with uranyl acetate and lead citrate. Images were acquired using a transmission electron microscope (FEI Tecnai Spirit Biotwin) operating at 100 kV.

Male fertility test

Males for fertility testing were raised under standard conditions. A single male was paired with three virgin w^{1118} females in a single tube for 7 days. If no larvae were observed, the male was considered sterile.

Drosophila Schneider 2 (S2) cell culture and immunoprecipitation

S2 cells (ATCC, CRL-1963) were cultured at 28 °C in Schneider's *Drosophila* medium (21720024, Gibco) supplemented with 10% fetal bovine serum (04–001-1ACS, Bioind). HA-Vha68-3 and Flag-Muc fusion proteins were expressed using the pUAS-attB plasmid. S2 cells were transfected using Effectene transfection reagent (301425, Qiagen). Immunoprecipitation was performed by extracting proteins from transfected cells, binding them to tag-labeled beads, and eluting for further analysis.

Western blot assay

Total protein was extracted from samples using RIPA lysis buffer (P0013D, Beyotime) supplemented with protease inhibitors. Proteins were separated by 12% sodium dodecyl sulfate (SDS) polyacrylamide gel electrophoresis (PAGE) and transferred onto nitrocellulose membranes. Membranes were blocked with 5% skimmed milk for 1 h at RT and incubated overnight at 4℃ with primary antibodies, including rabbit anti-Vha68-3 (1:1000, Yu lab), mouse anti-Tubulin (1:1000, AT819, Beyotime), rabbit anti-HA (1:1000, #3724 T, CST), and mouse anti-Flag (1:1000, AF519, Beyotime). After washing, membranes were incubated with fluorescent secondary antibodies (Alexa Fluor® 680, ab175773, Abcam; IRDye® 800, ab216772, Abcam) and visualized using an Amersham Typhoon 5 biomolecular imager (GE Healthcare Lifescience). ImageJ software was used for analysis.

Anti-Vha68-3 antibody preparation

Anti-Vha68-3 antibodies were developed by ABclonal Biotechnology. The Vha68-3 peptide (ASNEDRARNSGSLNQD-C) was synthesized and conjugated to Keyhole Limpet Hemocyanin (KLH). Antibodies were affinity purified using peptide-specific columns.

LC–MS/MS analysis

For in-gel digestion, gel particles were obtained from the entire gel, and cut into 1 mm^3 blocks and sequentially washed with water, 50% ACN, and 100% ACN. The gel particles were reduced with dithiothreitol (DTT), alkylated with iodoacetamide, and digested with trypsin at 37 °C for 12 h. After stopping the digestion with trifluoroacetic acid

(TFA), peptides were extracted from the gel particles, then desalted using StageTip (Thermofisher) before mass spectrometric (MS) analysis. For MS analysis, the purified peptides were resuspended in 0.1% formic acid (FA), separated on an analytical column (75 μm × 160 mm, 1.9 μm, Dr. Maisch), and analyzed using an Orbitrap Fusion Lumos mass spectrometer (Thermofisher) equipped with Easy-nLC 1200 system (Thermofisher). The data-dependent acquisition (DDA) mode was applied, while MS1 data were obtained in the Orbitrap with mass range of 350–1500 using 60k resolution, and MS/MS was performed by high-energy dissociation (HCD) in the Orbitrap with a resolution of 15k. MaxQuant software (version 1.6.5.0) was used for searching the raw files against the *Drosophila* melanogaster proteome database (downloaded June 2021). Identified peptides and proteins were filtered at a false discovery rate (FDR) of 1%. Searches were performed using Trypsin/P enzyme specificity while allowing up to two missed cleavages. Carbamidomethylation of cysteine residues (+57.0215 Da) was set as fixed modifications. Variable modifications included oxidation of methionines and acetylation of protein N termini. Enrichment analysis was performed using the STRING database [24].

Docking and interaction analysis

The tertiary structures of proteins were obtained from the PDB or AlphaFold databases, while small molecule structures were retrieved from PubChem. Robetta was used for predicting three-dimensional (3D) structures, HawkDock for protein–protein interactions, and CB-Dock2 for protein–small molecule interactions. Complexes were visualized using PyMOL.

Mitochondrial metabolism indicators

Mitochondrial metabolism indicators, including PA (BC2205, Solario), ATP (S0026, Beyotime), PDH (BC0385, Solario), and NAD+/NADH (S0175, Beyotime), were measured using tissue homogenates following the manufacturer's instructions. The resulting supernatants and detection reagents were transferred to a 96-well plate for the respective assays. The absorbance readings for the different experiments were taken as follows: PA at $\lambda = 520$ nm, PDH at $\lambda = 605$ nm, and NAD+/NADH at $\lambda = 450$ nm, utilizing a FlexStation 3 multimode microplate reader. The relative ATP levels were determined using a microplate reader from BioTek Instruments Inc.

Dietary supplementation

In dietary supplementation experiments, PA, SLG, and PEP were added to cornmeal medium at final concentrations of 2.5, 5.0, and 7.5 μg/mL. Flies were fed this supplemented medium for 40 days.

Single-cell suspensions, library preparation, and sequencing

Single-cell suspensions were prepared as previously described [25]. Approximately 150 male *Drosophila* testes (40 days) per sample were enzymatically dissociated and processed using a Singleron PythoN™ automated tissue dissociation system at 28 °C for a duration of 15 min. The resultant homogenate underwent centrifugation at 500*g* for 5 min and was subsequently resuspended in PBS. Assessment of cellular viability was conducted via Trypan Blue (Sigma-Aldrich) staining under microscopic observation. Subsequently, the single-cell suspensions were introduced into microfluidic devices utilizing a Singleron Matrix® single-cell processing system. Sequencing libraries were constructed using the GEXSCOPE® single-cell RNA library kit (Singleron Biotechnologies) and sequenced on an Illumina Novaseq 6000 platform.

Bioinformatics analysis of scRNA-seq

Raw sequencing reads were processed using Cell Ranger (version 3.1.0). Reads featuring substandard barcodes were eliminated, and unique molecular identifiers (UMIs) were sieved and aligned to the reference *Drosophila* melanogaster genome (Ensembl_release102). UMI count matrices corresponding to each cell barcode were utilized for subsequent analyses. Cells exhibiting abnormally high UMI counts (> 43,000) or mitochondrial gene percentages (> 25%) were excluded. Furthermore, cells detecting fewer than 820 or more than 5300 genes were also omitted. Seurat (version 3.1.1) was used for clustering and downstream exploration. Differentially upregulated genes were identified as statistically significant with a threshold criterion of ln(fold change) > 0.25 and *P*-value < 0.05. Differentially expressed genes (DEGs) were deemed significant with a fold change > 2 and *P*-value < 0.05. Gene Ontology (GO) and Kyoto Encyclopedia of Genes and Genomes (KEGG) analyses were performed using clusterProfiler. Single-cell trajectory analysis was conducted with Monocle 2 (version 2.10.1) to delve deeper into germ cell differentiation trajectories, pinpointing key factors essential for distinct stages during spermatogenesis.

Transcriptome–metabolomics association analysis

Fly tissues from the respective groups were used for both metabolomics and transcriptome analyses. Transcriptome profiling followed the methodology described in a previous publication [19]. Genes with a fold change greater than 2 and a false discovery rate (FDR) below 0.05 were identified as DEGs between the groups. For nontargeted metabolomics, following preprocessing, metabolites were detected through ultrahigh-performance liquid chromatography (UHPLC, 1290 Infinity LC; Agilent Technologies) coupled to a quadrupole time-of-flight (AB Sciex TripleTOF 6600). The raw MS data were converted to MzXML files using ProteoWizard MSConvert (version 3.0.6428) before importing into freely available XCMS software (online 3.7.1). In the extracted ion features, only variables having more than 50% of the nonzero measurement values in at least one group were kept. Metabolites were identified by comparing their mass and MS/MS data with those in mzCloud database which built from standard compounds, mzVault, and MassList databases. Both positive ion mode (POS) and negative ion mode (NEG) were employed to maximize metabolite coverage and detection efficiency. Data normalization was performed using *z*-scores, and hierarchical clustering was carried out with the R package pheatmap. Correlation analysis and heatmap visualizations were also performed using R and the pheatmap package. OPLS-DA, a variant of partial least squares discriminant analysis (PLS-DA) that incorporates an orthogonal signal correction (OSC) filter, was used to further analyze the data [26]. The VIP score from the OPLS-DA model was used to rank metabolites that distinguished between the two groups. Metabolites with a *t*-test *P*-value < 0.05 and VIP score ≥ 1 were considered differentially significant between the groups.

To integrate metabolomics and transcriptomics data, Pearson correlation coefficients were computed. Enriched pathways representing corresponding DEGs and differential metabolites were selected for heatmap analysis using the pheatmap package in R. In correlation-based clustering heatmaps, red indicated positive correlations while blue represented negative correlations. The intensity of the color indicated the strength of the correlation, with white asterisks denoting correlations with *P*-value < 0.05. Interaction network diagrams between DEGs and differential metabolites were generated using Cytoscape. Positive correlations are shown with red lines, while negative correlations are represented by green lines. DEGs and metabolites upregulated in the experimental group are marked in red, and downregulated ones in green. The intensity of the color of the circles or squares corresponded to the magnitude of fold change, while their size was proportional to the significance of the *P*-value.

Statistical analysis

All results are presented as mean ± standard error of the mean (SEM). Statistical analyses were performed using GraphPad Prism software version 6.01. For comparisons between two groups, Student's *t*-test was used for parametric analyses. For comparisons among multiple groups, one-way analysis of variance (ANOVA) was applied, followed by Dunnett's multiple comparisons test for post hoc analysis. For nonparametric analysis, the chi-squared (Fisher's exact) test was applied to assess rate comparisons. Statistical significance is denoted as follows: $^{*}P < 0.05$; $^{**}P < 0.01$; $^{***}P < 0.001$.

Results

Testis-specific Vha68-3 constitutes a crucial age-dependent factor influencing male fertility

Using the Fly Cell Atlas, a comprehensive transcriptomic repository of adult *Drosophila* tissues [27], we identified that *Vha68-3* is predominantly expressed in the testes, with its expression levels being particularly elevated in spermatids (Supplementary Fig. S1A). To investigate the role of Vha68-3 in testicular function, we generated *Vha68-3* knockout (KO) flies via CRISPR/Cas9, resulting in a 307-base pair (bp) deletion in the coding sequence (equivalent to a 384 bp deletion in the genome) (Fig. 1A). The KO was validated using PCR, sequencing (Fig. 1A; Supplementary Fig. S1B), and confirmed by the absence of the Vha68-3 protein as detected by specific antibodies (Supplementary Fig. S1C).

Fertility assessments revealed an age-dependent decline in male fertility in *Vha68-3* KO flies (Fig. 1B). At 2 days old, KO flies displayed no significant impact on fertility (fertility rate: control group 100%, $n = 50$; KO group 100%, $n = 55$). However, by 40 days of age, KO flies exhibited a significant reduction in fertility compared with controls (fertility rate: control group 100%, $n = 60$; KO group 26.7%, $n = 60$). DNA staining of testicular apexes revealed pronounced morphological abnormalities in the testes of 40-day-old KO flies, in contrast to controls (Fig. 1C). Phase-contrast microscopy further confirmed extensive damage to spermatogenic cells, particularly elongated spermatids, in the 40-day-old KO testes (Fig. 1D). The occurrence of dysmorphic testes peaked at 84% ($n = 106$) in 40-day-old KO flies, while no such abnormalities were detected in controls

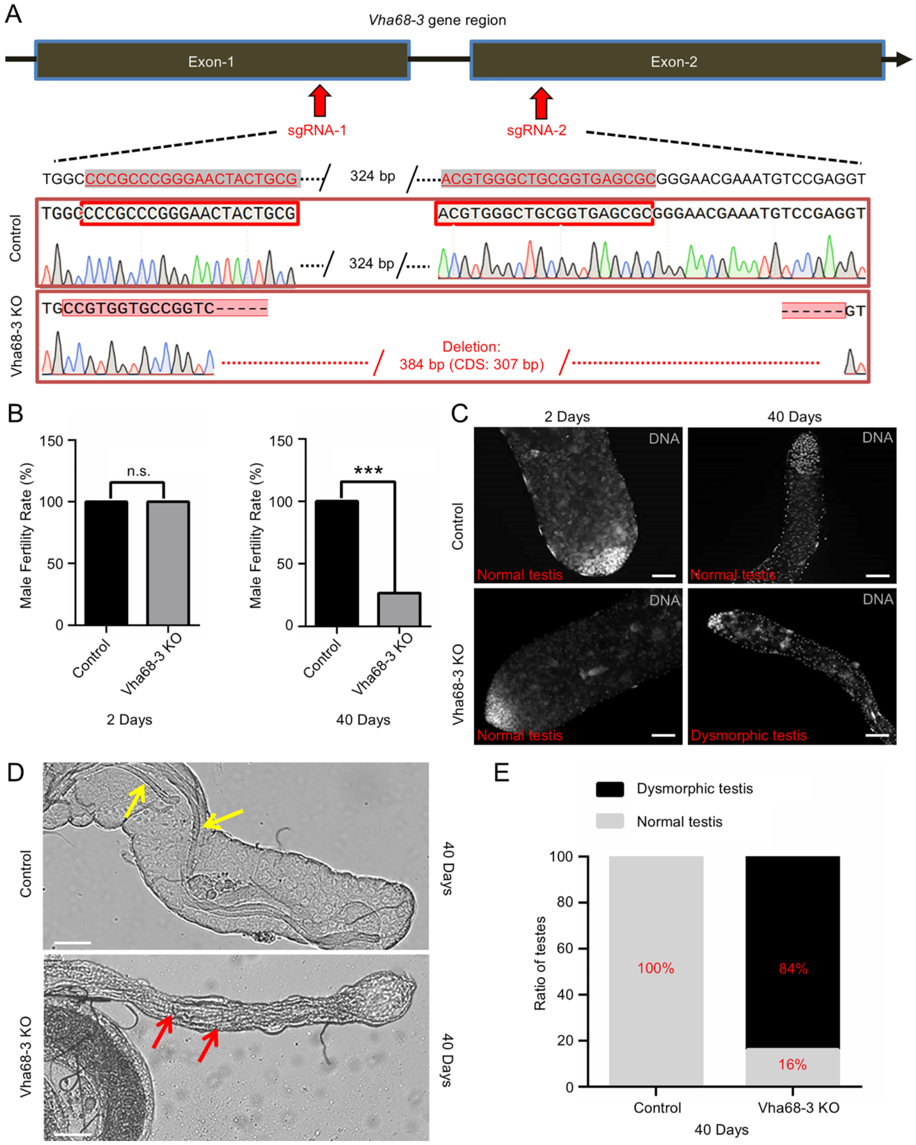

Fig. 1 *Vha68-3* deletion leads to spermiogenesis and male fertility defects during testicular aging. **A** Schematic representation of generating *Vha68-3* KO flies using CRISPR/Cas9 technology. **B** Comparison of male fertility between control and *Vha68-3* KO flies at 2 days ($n = 50$ for control; $n = 55$ for KO) and 40 days ($n = 60$ for control; $n = 60$ for KO) of age. **C** DNA staining at the testicular apex of control and *Vha68-3* KO groups at 2 days and 40 days of age. **D** Phase-contrast images of testes in control and *Vha68-3* KO flies at 40 days of age. Yellow arrows indicate normal elongated spermatid clusters, while red arrows denote defective elongated spermatid clusters. **E** Incidence of dysmorphic testes in control and *Vha68-3* KO groups at 40 days of age. Chi-squared (Fisher's exact) test; $^{***}P < 0.001$; scale bar: 50 μm

($n = 102$), consistent with the observed decline in fertility (Fig. 1B, E). These results suggest that the age-dependent fertility decline associated with Vha68-3 is likely due to spermatogenic dysfunction during testicular aging.

Vha68-3 regulates spermatid elongation during testicular aging

Immunofluorescence staining localized Vha68-3 primarily to the tails of elongated spermatids (Fig. 2A, B). In KO testes, the absence of Vha68-3 confirmed the successful KO

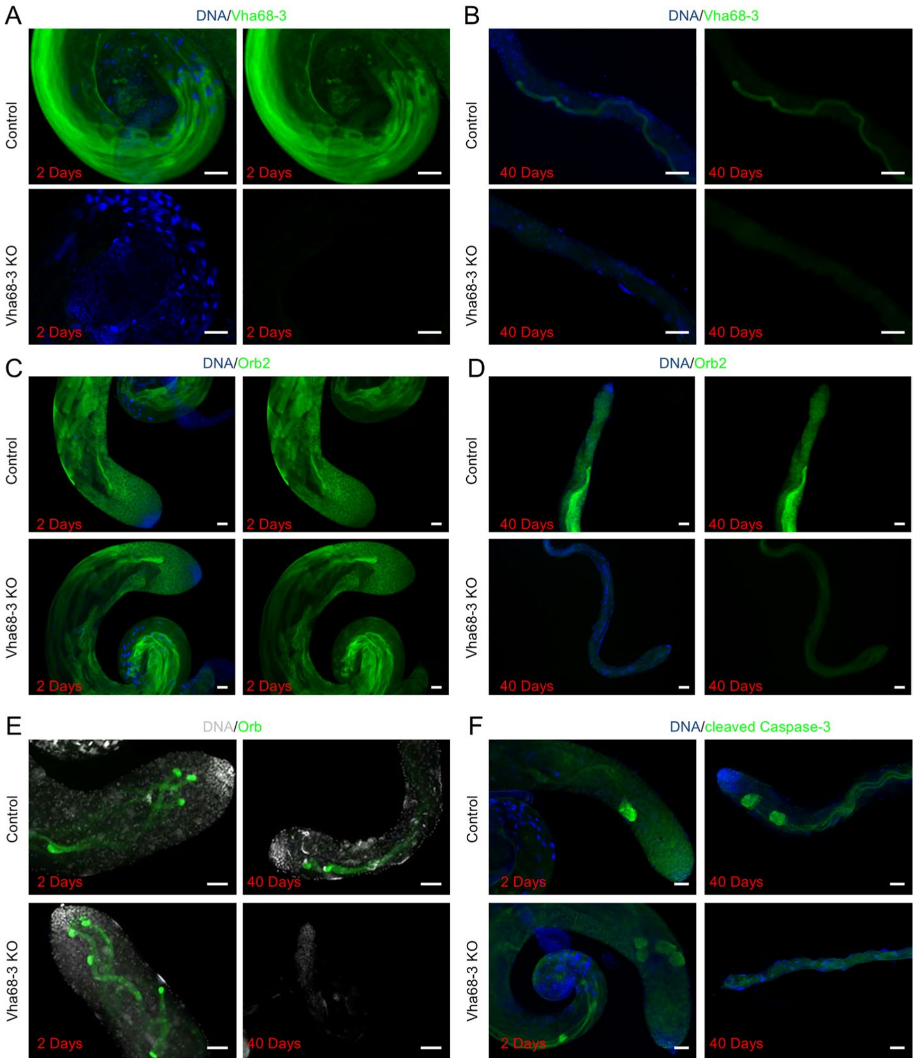

Fig. 2 *Vha68-3* deletion affects spermatid elongation. **A** Immunostaining for Vha68-3 (green) in control and *Vha68-3* KO testes at 2 days. **B** Immunostaining for Vha68-3 (green) in control and *Vha68-3* KO testes at 40 days. **C** Immunostaining for Orb2 (green) in control and *Vha68-3* KO testes at 2 days. **D** Immunostaining for Orb2 (green) in control and *Vha68-3* KO testes at 40 days. **E** Immunostaining for Orb (green) in control and *Vha68-3* KO testes at 2 and 40 days. **F** Immunostaining for cleaved Caspase-3 (green) in control and *Vha68-3* KO testes at 2 and 40 days. DNA stained with Hoechst 33342; scale bar: 50 µm

at the protein level (Fig. 2A, B). Interestingly, a decline in Vha68-3 expression was also observed as the testes aged (Fig. 2A, B). Significantly, in *Vha68-3* KO testes, the oo18 RNA-binding protein (Orb) and Orb2 proteins, crucial markers of spermiogenesis, exhibited no alterations at 2 days but were notably absent in the tails of elongated spermatids at 40 days when compared with control testes (Fig. 2C–E; Supplementary Fig. S2A, B). Caspase activation assays also revealed that, while cleaved-Caspase-3 signals were normal in both 2-day-old control and KO testes, by 40 days of age, *Vha68-3* deficiency resulted in the loss of CB and WB structures, contrasting with their presence in 40-day-old controls (Fig. 2F; Supplementary Fig. S2C, D). Moreover, we observed reductions in both punctate and branched fusomes, indicative of undifferentiated and differentiated stages of germ cells, respectively, at the apex of the 40-day-old KO testes

(Supplementary Fig. S3A–C). Additionally, mature cyst cells (identified by Eya) and early-stage cyst cells (identified by Tj) also exhibited a degree of reduction at the apex of the KO testes by the 40th day (Supplementary Fig. S3D–G). On the basis of our current findings, it is suggested that Vha68-3 may orchestrate a complex regulatory network across multiple cell types during testicular aging, with an essential involvement in regulating spermatid elongation.

Vha68-3 controls mitochondrial function in elongated spermatids during testicular aging

V-type ATPase is known to localize primarily to membranous structures, such as lysosomes [28]. Initially, we investigated whether Vha68-3 affected lysosome-related processes in the testes. Co-localization analysis of Vha68-3 and Lyso-Tracker revealed no lysosomal presence at the tails of elongated spermatids (Fig. 3A). Prior evidence suggests a link between V-type ATPase and mitochondrial function [29], leading us to hypothesize that *Vha68-3*, as a testis-specific V-type ATPase subunit, regulates spermatid elongation via mitochondrial derivatives. To test this, we used Translocase of the Outer Membrane 20 (Tom20) and Bellwether (Blw, also known as ATP5A) as mitochondrial markers. Strikingly, we observed a marked reduction in mitochondrial signal intensity during testicular aging, with distinct mitochondrial abnormalities in elongated spermatids only evident in the 40-day-old KO testes (Fig. 3B, C; Supplementary Fig. S4A–D). These findings highlight the critical role of Vha68-3 in maintaining mitochondrial function during testicular aging.

To further examine the subcellular impact of *Vha68-3* deficiency, we performed transmission electron microscopy (TEM). TEM analysis of 2-day-old testes showed no differences in major and minor mitochondrial derivatives or axonemal structures between control and KO groups (Fig. 3D; Supplementary Fig. S4E). However, in 40-day-old testes, while axonemal structures remained intact, the major mitochondrial derivatives in KO testes exhibited swelling and severe damage, with dispersed paracrystalline contents, and the minor mitochondrial derivatives were entirely absent (Fig. 3D; Supplementary Fig. S4F). These data demonstrate that Vha68-3 plays a pivotal role in maintaining mitochondrial integrity and homeostasis during testicular aging.

Vha68-3-mediated testicular transcriptional landscape at single-cell resolution

To investigate the role of Vha68-3 in testicular development, we characterized cells using scRNA-seq from freshly dissected testes of both control and *Vha68-3* KO groups (40 days old). Approximately 150 testes (40 days) were mixed in a sample. On average, each cell displayed 10,359.5 unique molecular identifiers (UMIs) and 2423 genes. After stringent filtering, 13,562 high-quality cells were selected for subsequent analysis. These cells could be distinctly categorized into somatic and germline populations (Fig. 4A). Two independent experiments for each group further confirmed the consistency of major cell clusters, demonstrating minimal batch effects while preserving the distinctions between control and KO groups (Fig. 4B).

Using uniform manifold approximation and projection (UMAP), we visualized ten distinct cell populations, encompassing all known cell types in *Drosophila* testes, which could be separated into germline and somatic clusters (Fig. 4C). To annotate these clusters precisely, we cross-referenced the expression of well-characterized marker genes,

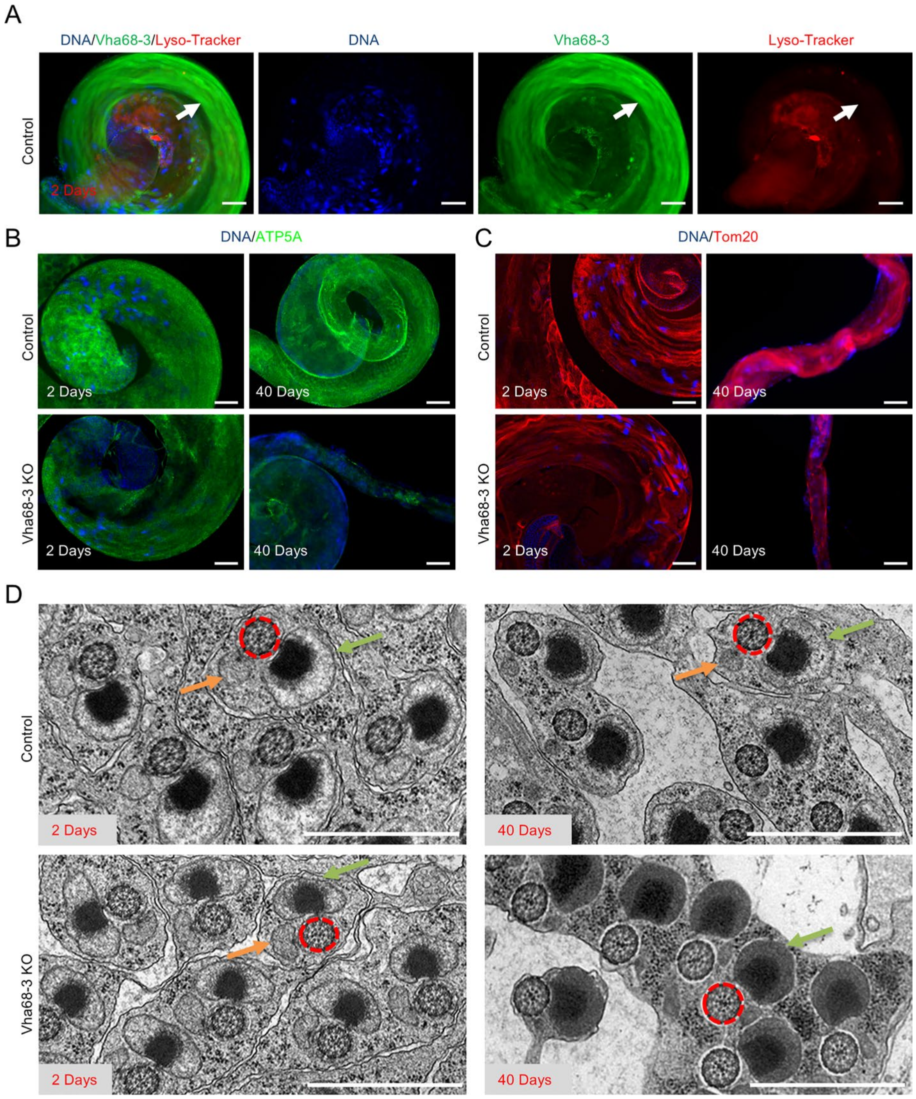

Fig. 3 *Vha68-3* deletion induces age-dependent mitochondrial defects in elongated spermatids. **A** Staining for Vha68-3 (green) and Lyso-Tracker (red) in 2-day-old control testes; white arrows indicate elongated spermatids. **B** Immunostaining for ATP5A (green) in control and *Vha68-3* KO testes at 2 and 40 days. **C** Immunostaining for Tom20 (red) in control and *Vha68-3* KO testes at 2 and 40 days. **D** TEM analysis of elongated spermatids in control and *Vha68-3* KO testes at 2 and 40 days. Red circles mark axonemes; green and orange arrows indicate major and minor mitochondrial derivatives, respectively. DNA stained with Hoechst 33342; scale bar: 50 µm for immunostainings, 1 µm for TEM images

using Dotplot analysis to confirm their identities (Fig. 4D; Supplementary Table S1). The representative marker genes, as previously reported [13, 25], were further mapped onto UMAP plots to visualize their distribution (Fig. 4E).

We then quantified RNA content and gene expression within each cluster by analyzing UMI count (nUMIs) and gene count (nGenes), revealing that germline clusters exhibited the highest levels of transcriptional activity among the annotated populations (Supplementary Fig. S5A, B). The most highly expressed genes for each cell population were highlighted (Supplementary Fig. S5C; Supplementary Table S2). Notably, we observed a significant enrichment of genes involved in mitochondrial function and spermiogenesis,

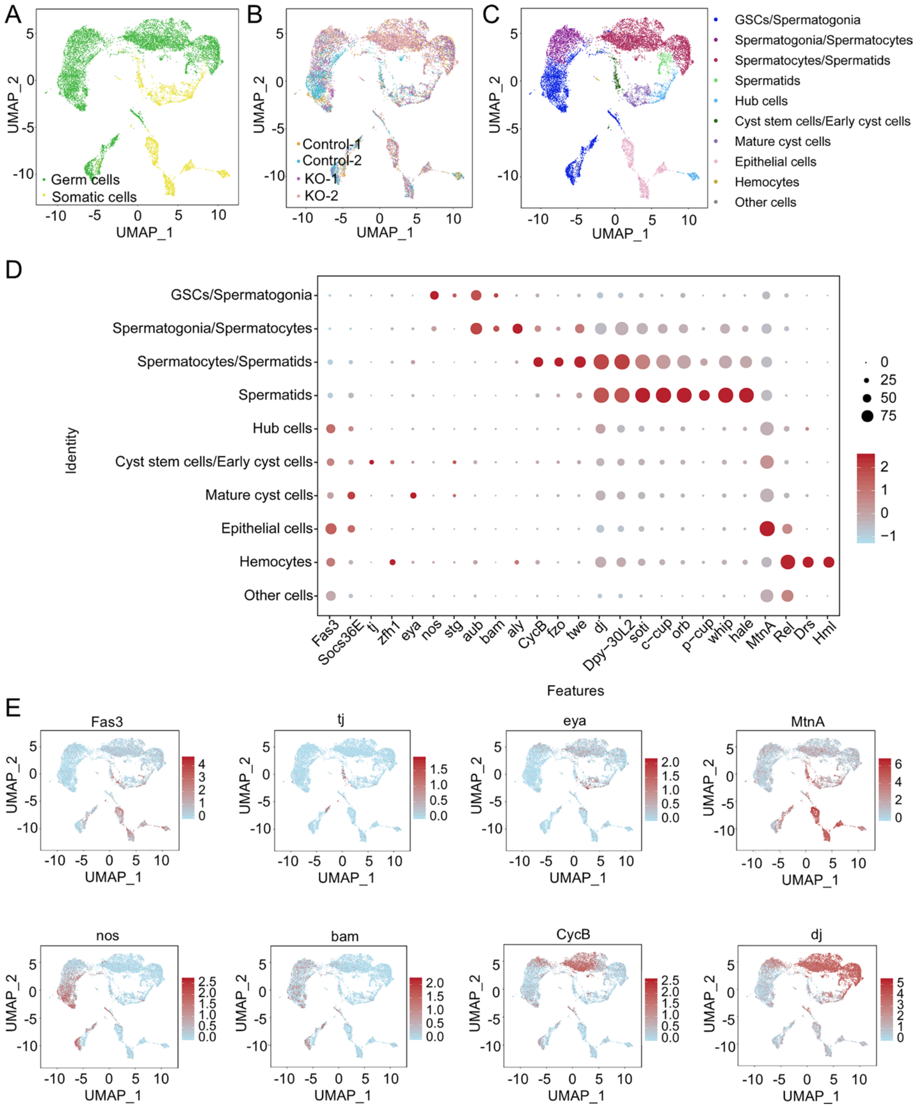

Fig. 4 scRNA-seq analysis of control and *Vha68-3* KO testes. **A** UMAP visualization of somatic and germline cell populations. **B** UMAP plot of testicular cells colored by sample. **C** UMAP plot of testicular cells colored by identified clusters. **D** Dot plot showing marker gene expression, with dot size indicating gene expression proportion and color intensity representing average expression levels. **E** UMAP visualization of representative marker genes

particularly within the Spermatocytes_Spermatids and Spermatids clusters. These genes were associated with key cellular components (e.g., mitochondrial membrane, cilium), biological processes (e.g., mitochondrial transport, spermatid differentiation), and molecular functions (e.g., tubulin binding, protein transmembrane transporter activity) (Supplementary Fig. S5D, E). KEGG pathway enrichment analysis further indicated the involvement of mitochondrial metabolic pathways, such as the tricarboxylic acid (TCA) cycle, pyruvate metabolism, and oxidative phosphorylation, in spermatid elongation (Supplementary Fig. S5F, G). Collectively, these findings suggest that metabolism shifts, including mitochondrial metabolisms, are significant during spermatid development.

Discovery of novel stages in testicular germ cell development

To explore the developmental trajectory of germ cell populations, we reclustered the germline cells and conducted pseudotime trajectory analysis (Supplementary Fig. S6A, B). This analysis revealed three novel developmental stages in testicular germ cell maturation, closely aligned with the established stages of spermatogenesis (Supplementary Fig. S6C, D). Cellular component analysis demonstrated that early-stage germ cells were predominantly localized to stage 2 and stage 3, while stage 1 was primarily associated with later stages of spermatogenesis (Supplementary Fig. S6E). Dotplot visualizations further highlighted genes enriched at each stage (Supplementary Fig. S6F). Importantly, several stage-specific genes were identified: *CG33668* for stage 1, *CG43057* for stage 2, and *piwi* for stage 3, shedding light on the complexity of germ cell development within the testes (Supplementary Fig. S6G, H).

To further investigate the molecular regulation across these stages, we identified differentially expressed genes (DEGs) through heatmap visualization (Supplementary Fig. S7A). Key DEGs, such as *CG45490*, *CG43120*, and *CG45154*, were critical for germline complexity and were further visualized in UMAP plots comparing control and KO germline populations at 40 days (Supplementary Fig. S7B–D). These findings provide valuable insights into the progressive differentiation of germline populations, elucidating the molecular mechanisms driving spermatogenesis and revealing new layers of complexity in testicular germ cell development.

Vha68-3-mediated transcriptional regulation in late-stage germline populations

To assess the impact of *Vha68-3* deficiency on transcriptional regulation in late-stage germline cells, we analyzed the DEGs within each testicular cell cluster at 40 days (Fig. 5A). This analysis focused on the Spermatocytes/Spermatids and Spermatids clusters, where significant DEGs were visualized in volcano plots (Fig. 5B, C). Notably, *CG45154* was upregulated following *Vha68-3* deficiency in both clusters, correlating with the enhanced germ cell complexity observed in the pseudotime trajectory analysis.

Gene Ontology (GO) and KEGG pathway enrichment analyses of late-stage germline cells further revealed significant enrichment of ATP synthase-related processes (e.g., proton-transporting V-type ATPase complex, proton-transporting ATP synthase activity) and metabolic pathways (e.g., oxidative phosphorylation) between control and *Vha68-3* KO testes (Fig. 5D, E; Supplementary Fig. S8). These findings suggest that Vha68-3 potentially regulates spermatid elongation via diverse transcriptional pathways. Our scRNA-seq analysis underscores the role of Vha68-3 in mitochondrial processes and other enriched pathways during the late stages of spermatogenesis.

Mitochondrial-related proteins are enriched for Vha68-3 binding proteins

To explore the regulatory network involving Vha68-3 binding proteins, we immunoprecipitated 3xHA-Vha68-3 fusion proteins using HA beads in unexpressed fusome proteins (control) and expressed fusome proteins (Vha68-3 OE) groups in *Drosophila* S2 cells (Fig. 6A), subsequently subjecting them to liquid chromatography-tandem mass spectrometry (LC–MS/MS). Vha68-3 binding proteins were identified with unique peptides and LFQ intensity (value of 0 in the control group and greater than 0 in the

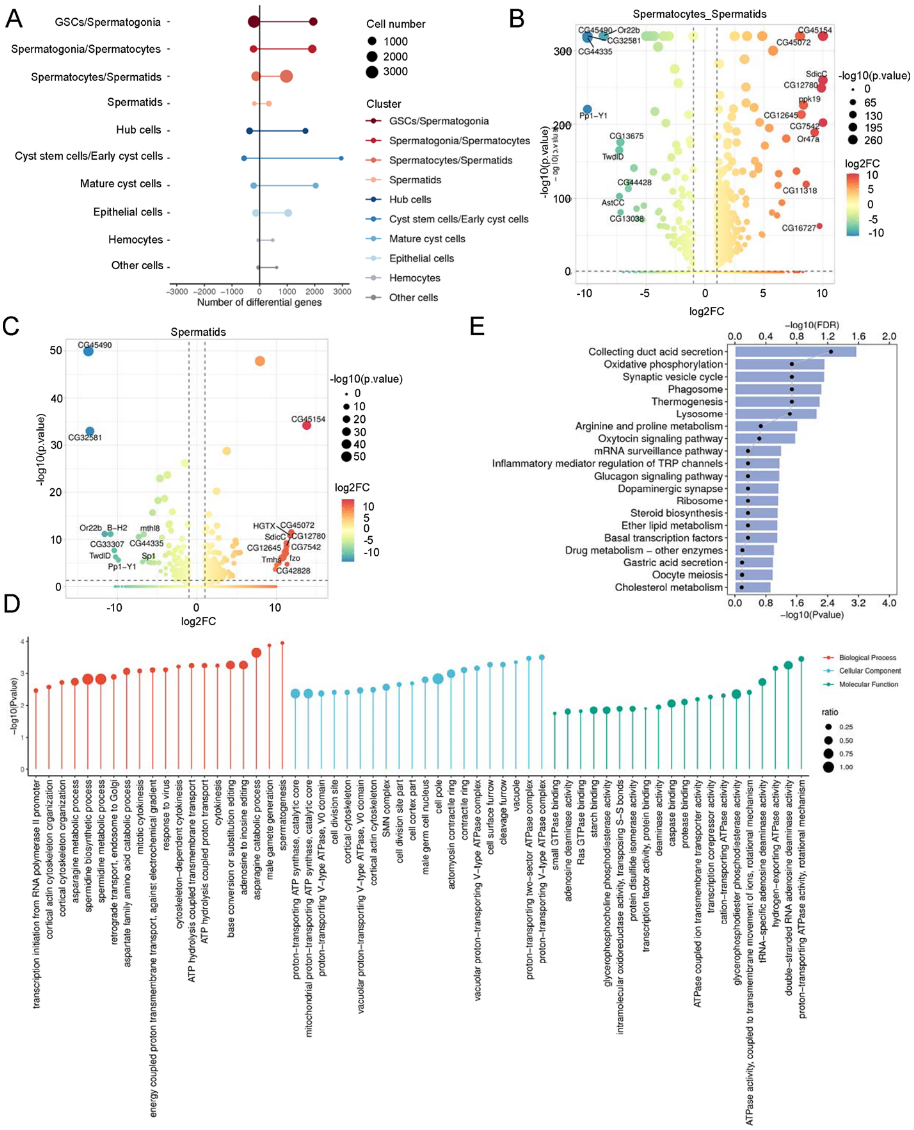

Fig. 5 DEGs and their enrichment in spermiogenesis mediated by *Vha68-3* deletion. **A** Number of DEGs in each cell cluster between control and *Vha68-3* KO testes. **B** Volcano plot showing DEGs in the Spermatocytes_Spermatids cluster. **C** Volcano plot showing DEGs in the Spermatids cluster. **D** GO enrichment analysis of DEGs in the Spermatids cluster. **E** KEGG pathway enrichment analysis of DEGs in the Spermatids cluster

Vha68-3 OE group), and ultimately discovered 39 Vha68-3 binding proteins in *Drosophila* (Fig. 6B; Supplementary Table S3). The proteins identified with unique peptides and LFQ intensity in both the control and Vha68-3 OE groups were classified as non-specific binding proteins. Functional enrichment analysis based on GO and Domains revealed that these proteins are primarily involved in mitochondrial regulation, V-type ATP synthase function, ATP binding, and related processes (Supplementary Fig. S9A, B). Integrated pathway analysis further highlighted the significant enrichment of Vha68-3 binding proteins in events related to V-type ATPase, pyruvate metabolism, and TCA cycle (Supplementary Fig. S9C). Protein–protein interaction (PPI) analysis uncovered a regulatory network in which Vha68-3 interacts with other Vha subunits, such as

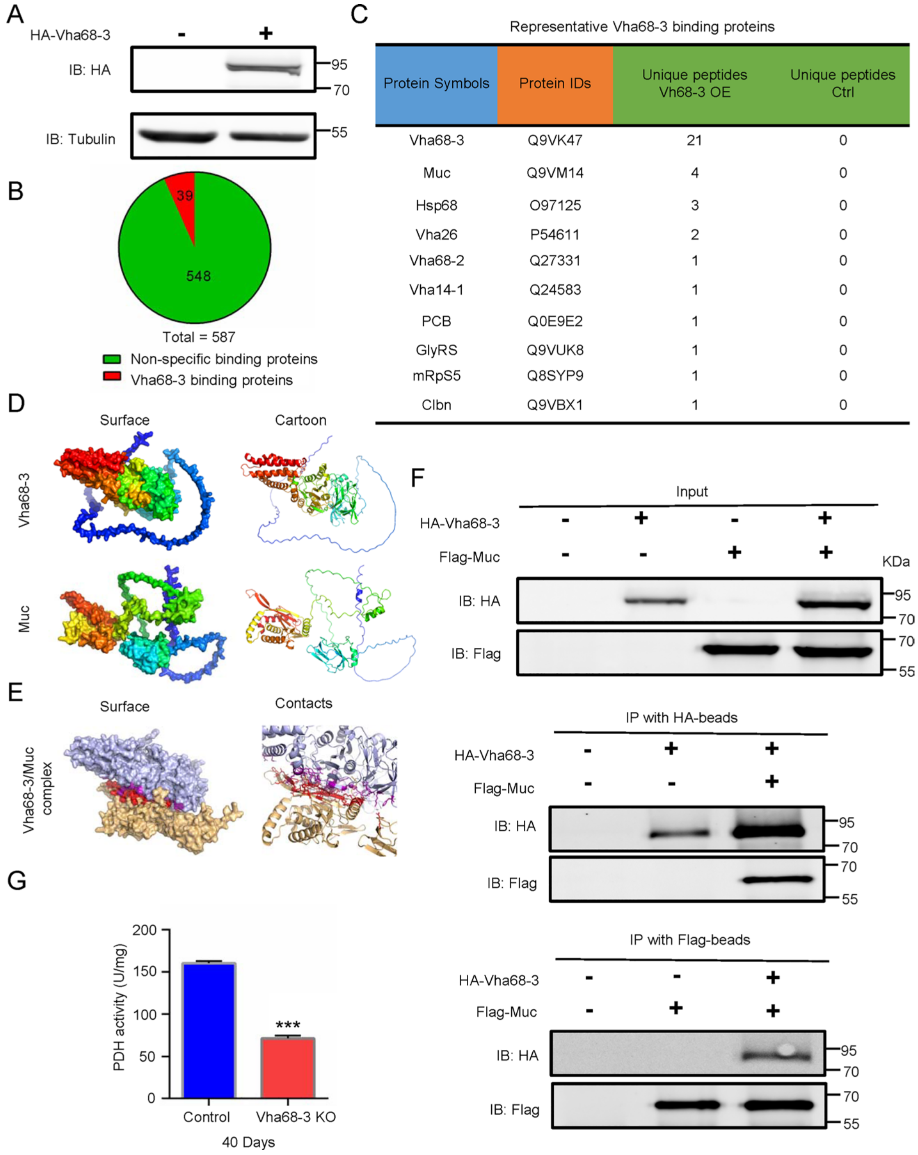

Representative Vha68-3 binding proteins

Protein Symbols	Protein IDs	Unique peptides Vh68-3 OE	Unique peptides Ctrl
Vha68-3	Q9VK47	21	0
Muc	Q9VM14	4	0
Hsp68	O97125	3	0
Vha26	P54611	2	0
Vha68-2	Q27331	1	0
Vha14-1	Q24583	1	0
PCB	Q0E9E2	1	0
GlyRS	Q9VUK8	1	0
mRpS5	Q8SYP9	1	0
Clbn	Q9VBX1	1	0

Fig. 6 Identification of Vha68-3 binding proteins. **A** Pull-down assay for Vha68-3 binding proteins. **B** Number of Vha68-3 binding proteins identified via LC–MS/MS. **C** Ten representative Vha68-3 binding proteins. **D** Three-dimensional structural models for Vha68-3 and Muc proteins. **E** Visualization of the docking interface for the Vha68-3/Muc complex. **F** Reciprocal co-IP of Vha68-3 and Muc proteins. **G** PDH activity in control ($n = 4$) and Vha68-3 KO ($n = 4$) testes at 40 days. Bars represent mean ± SEM; Student's *t*-test; ***$P < 0.001$

Vha68-2, Vha26, and Vha14-1 (Supplementary Fig. S9D). Among these, the top ten most representative Vha68-3 binding proteins were highlighted, with a particular focus on the Midline uncoordinated (Muc) protein (Fig. 6C). Therefore, we next investigated relationship between Vha68-3 and Muc.

We further determined the three-dimensional structures of Vha68-3 and Muc using Robetta, a tool for predicting protein structures on the basis of co-evolutionary data [30] (Fig. 6D). Leveraging these structural models, we predicted the Vha68-3/Muc complex using HawkDock [31], and visualized the interaction using PyMOL (https://pymol.org/2/) (Fig. 6E). Supplementary Table S4 details the critical residues involved in the Vha68-3/Muc interaction. To confirm the physiological relevance of these interactions, we conducted co-immunoprecipitation (co-IP) assays, which verified the binding between Vha68-3 and Muc (Fig. 6F). Furthermore, we revealed a significant decrease in pyruvate dehydrogenase (PDH) activity, an indicator important for pyruvate metabolism, in *Vha68-3* KO testes at 40 days compared with controls (Fig. 6G). Taken together, these findings provide additional evidence supporting the notion that Vha68-3 may play a role in mitochondrial metabolism.

Transcriptome–metabolomics association analysis reveals the involvement of Vha68-3 in mitochondrial metabolism

To further delineate the transcriptional and metabolic networks regulated by Vha68-3, we conducted a transcriptome–metabolomics association analysis in 40-day-old control and *Vha68-3* KO flies. Using orthogonal projection to latent structures-discriminant analysis (OPLS-DA) of the nontargeted metabolomics dataset, we identified 166 upregulated and 149 downregulated metabolites (Fig. 7A–C; Supplementary Table S5). The top 100 metabolites influenced by *Vha68-3* KO were visualized via a correlation heatmap (Supplementary Fig. S10). Moreover, we highlighted representative differential metabolites with high variable importance in projection (VIP) values, noting decreases in multiple metabolites, including pyruvate (PA), following *Vha68-3* deficiency at 40 days compared with the control group (Fig. 7D). The KEGG pathway analysis further unveiled extensive metabolic perturbations encompassing cyanoamino acid metabolism, glycine, serine, and threonine metabolism, biosynthesis of amino acids, pyruvate metabolism, folate biosynthesis, carbon metabolism, citrate cycle (TCA cycle), and other pathways, which were enriched among the differential metabolites between the control and *Vha68-3* KO groups at 40 days (Fig. 7E). While pyruvate does not rank as the most significantly altered metabolite in our metabolome dataset, it is noteworthy that both omics analysis and functional experiments in this study have substantiated the potential significance of mitochondrial-associated metabolism in *Vha68-3* KO flies. Therefore, we further investigated the mitochondrial metabolism related indicators, and showed partial but not complete decline in ATP and PA levels, alongside elevated NADH, decreased NAD+, and a lower NAD+/NADH ratio in the *Vha68-3* KO flies at 2 days, suggesting residual metabolic activity (Supplementary Fig. S11). However, these compensatory mechanisms may fail, leading to accelerated alterations of mitochondrial related indicators in the Vha68-3 KO flies at 40 days (Fig. 7F–J). These metabolomic findings indicate that Vha68-3 is involved in the regulation of diverse metabolic processes, encompassing mitochondrial metabolism, during spermatid elongation and testicular aging.

Transcriptomic analysis between control and *Vha68-3* KO flies at 40 days identified 1348 DEGs, with 416 upregulated and 932 downregulated genes (Supplementary Table S6). A volcano plot highlighted notable DEGs, including the upregulated gene *CG45154* (Supplementary Fig. S12A). GO enrichment analysis indicated that the DEGs were involved in diverse cellular components, molecular functions, and biological processes, such as proteolysis, reproductive behavior, ion transport regulation, transporter complexes, peptidase activity, and channel activity (Fig. S12B). KEGG analysis further revealed that *Vha68-3* deficiency impacted metabolic pathways,

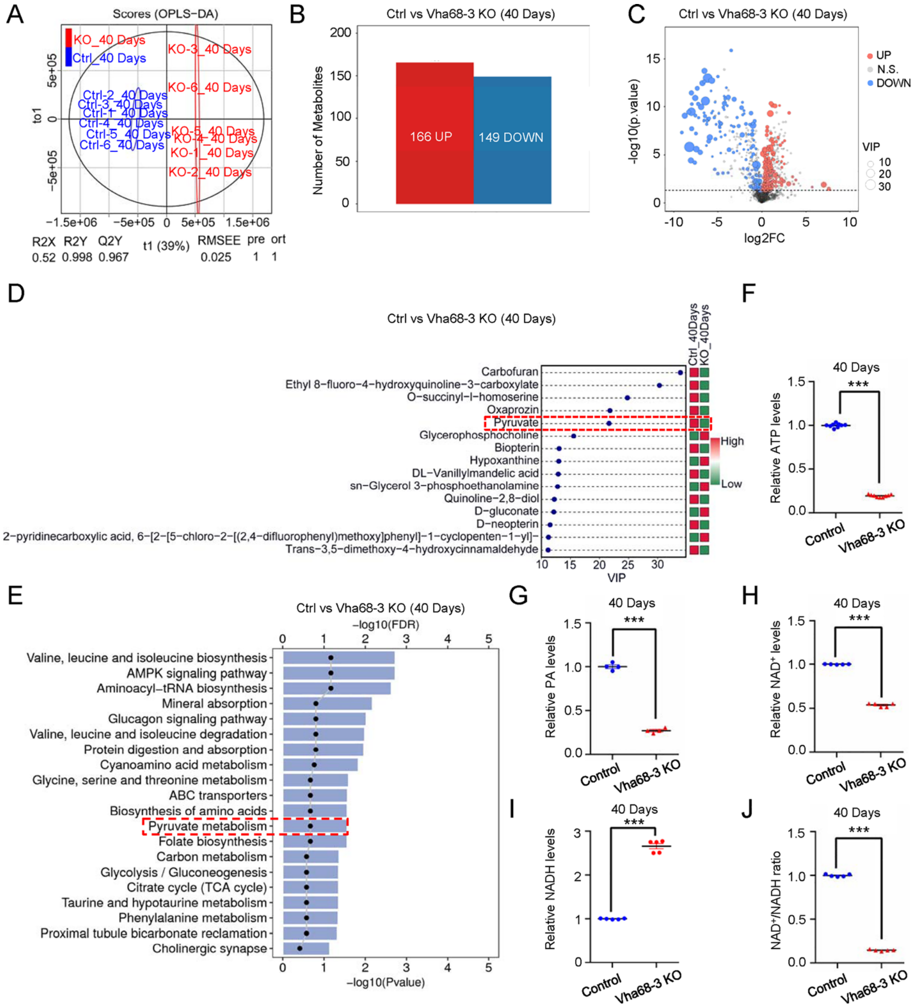

Fig. 7 Metabolomics analysis of *Vha68-3* deletion. **A** OPLS-DA score plot comparing control and *Vha68-3* KO groups at 40 days. **B** Number of differential metabolites between 40-day-old control and *Vha68-3* KO groups. **C** Volcano plot of differential metabolites. **D** Representative differential metabolites with high VIP values. **E** Metabolic pathway enrichment analysis. **F** Relative levels of ATP in control ($n = 9$) and Vha68-3 KO ($n = 9$) groups at 40 days. **G** Relative levels of PA in control ($n = 4$) and Vha68-3 KO ($n = 4$) groups at 40 days. **H-J** Relative levels of NAD+, NADH, and NAD+/NADH ratio in control ($n = 5$) and Vha68-3 KO ($n = 5$) groups at 40 days. Bars represent mean ± SEM; Student's *t*-test; ***$P < 0.001$

including cytochrome P450, pentose and glucuronate interconversions, ascorbate and aldarate metabolism, arginine and proline metabolism, glutathione metabolism, and folate biosynthesis (Fig. S12C).

Integrated transcriptome and metabolome analysis uncovered enriched pathways and associated differential metabolites and DEGs between control and *Vha68-3* KO groups (Fig. 8A, B). Notably, metabolites such as indole-3-pyruvic acid, indolelactic acid, hydroxyphenyllactic acid, *O*-succinyl-L-homoserine, 3-phospho-D-glycerate, α-ketoisovaleric acid, phenylpyruvate (PP), phosphoenolpyruvate (PEP), PA, and *S*-lactoylglutathione (SLG) were all decreased in the *Vha68-3* KO group (Fig. 8C). Correlation-based clustering heatmaps and interaction network diagrams illustrated

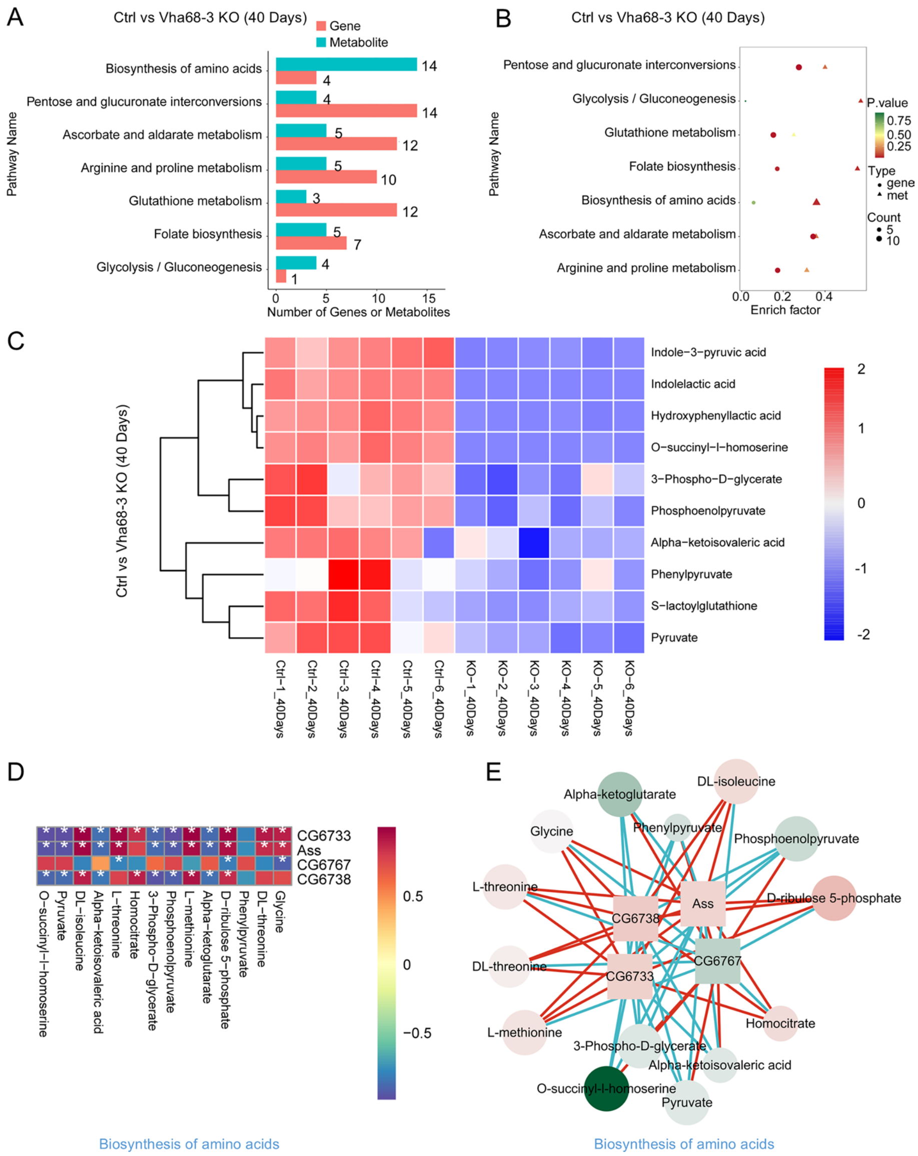

Fig. 8 Transcriptome–metabolomics association analysis for *Vha68-3* deletion-mediated regulatory networks. **A** Numbers of distinct metabolites and DEGs identified in various pathways. **B** Enrichment analysis for core pathways. **C** Heatmap showing differential metabolites. **D** Correlation-based clustering heatmap of metabolites and DEGs in the biosynthesis of amino acids pathway. **E** Interaction network diagram of metabolites and DEGs in the biosynthesis of amino acids pathway

relationships between differentially expressed metabolites and genes, particularly in pathways involved in biosynthesis of amino acids, glycolysis/gluconeogenesis, folate biosynthesis, ascorbate and aldarate metabolism, pentose and glucuronate interconversions, arginine and proline metabolism, and glutathione metabolism, that predominantly govern the regulation of mitochondrial metabolic processes (Fig. 8D, E; Supplementary Fig. S13).

Mitochondrial metabolism-associated compounds mitigate spermatid elongation defects induced by *Vha68-3* deficiency during testicular aging

To assess the therapeutic potential of modulating mitochondrial metabolism, we administered dietary compounds of PA, SLG, and PEP, which were three downregulated metabolites identified in the *Vha68-3* KO group. This intervention aimed to mitigate spermatid elongation defects and restore mitochondrial function during testicular aging. The three-dimensional structures of Vha68-3 were analyzed for potential binding pockets (Fig. 9A, B), and interaction predictions between Vha68-3 and PA, SLG, or PEP were conducted using CB-Dock2 [32]. The key residues at the interface of Vha68-3 and these metabolites were visualized (Fig. 9C; Supplementary Fig. S14; Supplementary Tables S7–S9).

In vivo experiments revealed partial rescue of spermatid elongation defects and increased numbers of Orb-positive spermatids following dietary supplementation with PA, SLG, and PEP in *Vha68-3* KO testes (Fig. 9D–G; Supplementary Fig. S15A–D). Additionally, Vha68-3 signals and ATP5A-labeled mitochondria were restored in elongated spermatids after treatment with these compounds (Fig. 9H; Supplementary Fig. S15E, F). Meanwhile, we also noticed that not all mitochondrial metabolism-associated metabolites could effectively alleviate spermatid elongation defects in *Vha68-3* KO testes. PP was identified with downregulation in *Vha68-3* KO group at 40 days (Fig. 8C; Supplementary Table S5), and exhibited potential roles in pyruvate metabolism [33, 34]. Following dietary supplementation with PP, *Vha68-3* deficiency mediated spermatid elongation defects could not be rescued (Fig. 9F, G). These findings provide new insights into strategies for mitigating mitochondrial metabolic disorders in elongated spermatids during testicular aging.

Discussion

Declines in sperm quality and male fertility resulting from abnormal spermiogenesis are hallmark features of testicular aging [35]. Testicular aging is closely associated with several factors, including genomic instability, mitochondrial dysfunction, stem cell exhaustion, epigenetic modifications, cellular senescence, telomere attrition, impaired macroautophagy, dysregulated nutrient sensing, proteostasis loss, chronic inflammation, altered intercellular signaling, and dysbiosis [36]. Our primary finding identifies Vha68-3, a testis-specific factor, as a critical aging-related regulatory element essential for maintaining mitochondrial derivative homeostasis in elongated spermatids during testicular aging, with its deficiency exacerbating age-related metabolic exhaustion (Fig. 10).

Mitochondria, acting as the central hub of cellular energy metabolism, play an indispensable role in spermatid elongation [37]. Given the high complexity of spermiogenesis, further investigation is required to explore the assembly and elongation of mitochondrial structures during this process. The challenge lies in unraveling the regulatory network that controls the functionality of mitochondria in elongated spermatids. In *Drosophila* testes, mitochondria aggregate and fuse to form the Nebenkern structure in round spermatids, eventually giving rise to two distinct mitochondrial derivatives during spermatid elongation: the major and minor mitochondrial derivatives [38]. The major mitochondrial derivative is distinguished by electron-dense

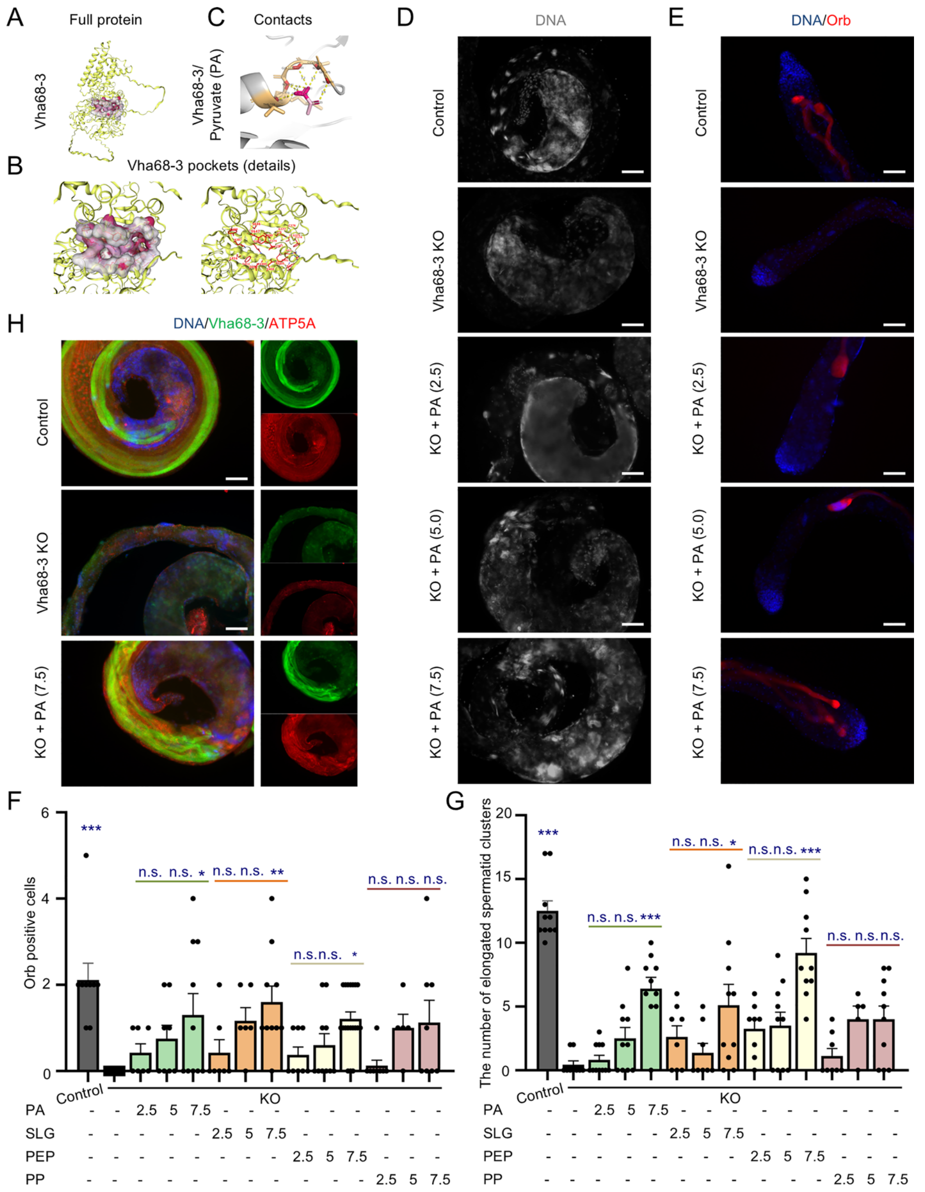

Fig. 9 Rescue assays with mitochondrial-related compounds in *Vha68-3* deletion-mediated spermiogenesis defects. **A** Three-dimensional structure of the Vha68-3 protein. **B** Visualization of Vha68-3 pockets. **C** Key residues at Vha68-3/PA interaction sites. **D** DNA stainings at the tails of testes in control, Vha68-3 KO, Vha68-3 KO + PA (2.5 μg/mL), Vha68-3 KO + PA (5.0 μg/mL), Vha68-3 KO + PA (7.5 μg/mL) groups (40 days). **E** Immunostainings of Orb (red) in control, Vha68-3 KO, Vha68-3 KO + PA (2.5 μg/mL), Vha68-3 KO + PA (5.0 μg/mL), Vha68-3 KO + PA (7.5 μg/mL) groups (40 days). **F** The number of Orb-positive cells in control (*n* = 9), Vha68-3 KO (*n* = 10), Vha68-3 KO + PA (2.5 μg/mL) (*n* = 7), Vha68-3 KO + PA (5 μg/mL) (*n* = 8), Vha68-3 KO + PA (7.5 μg/mL) (*n* = 10), Vha68-3 KO + SLG (2.5 μg/mL) (*n* = 7), Vha68-3 KO + SLG (5 μg/mL) (*n* = 6), Vha68-3 KO + SLG (7.5 μg/mL) (*n* = 10), Vha68-3 KO + PEP (2.5 μg/mL) (*n* = 8), Vha68-3 KO + PEP (5 μg/mL) (*n* = 10), Vha68-3 KO + PEP (7.5 μg/mL) (*n* = 19), Vha68-3 KO + PP (2.5 μg/mL) (*n* = 8), Vha68-3 KO + PP (5 μg/mL) (*n* = 5), Vha68-3 KO + PP (7.5 μg/mL) (*n* = 8) groups. **G** The number of elongated spermatid clusters in control (*n* = 10), Vha68-3 KO (*n* = 9), Vha68-3 KO + PA (2.5 μg/mL) (*n* = 11), Vha68-3 KO + PA (5 μg/mL) (*n* = 10), Vha68-3 KO + PA (7.5 μg/mL) (*n* = 10), Vha68-3 KO + SLG (2.5 μg/mL) (*n* = 8), Vha68-3 KO + SLG (5 μg/mL) (*n* = 8), Vha68-3 KO + SLG (7.5 μg/mL) (*n* = 10), Vha68-3 KO + PEP (2.5 μg/mL) (*n* = 8), Vha68-3 KO + PEP (5 μg/mL) (*n* = 10), Vha68-3 KO + PEP (7.5 μg/mL) (*n* = 10), Vha68-3 KO + PP (2.5 μg/mL) (*n* = 8), Vha68-3 KO + PP (5 μg/mL) (*n* = 5), Vha68-3 KO + PP (7.5 μg/mL) (*n* = 10) groups. **H** Immunostainings of Vha68-3 (green) and ATP5A (red) in control, Vha68-3 KO and Vha68-3 KO + PA (7.5 μg/mL) testes (40 days). DNA is stained with Hoechst 33342 in testes. Bars represent mean ± SEM; one-way ANOVA with Dunnett's multiple comparisons test; *$P < 0.05$, **$P < 0.01$, ***$P < 0.001$; scale bar: 50 μm

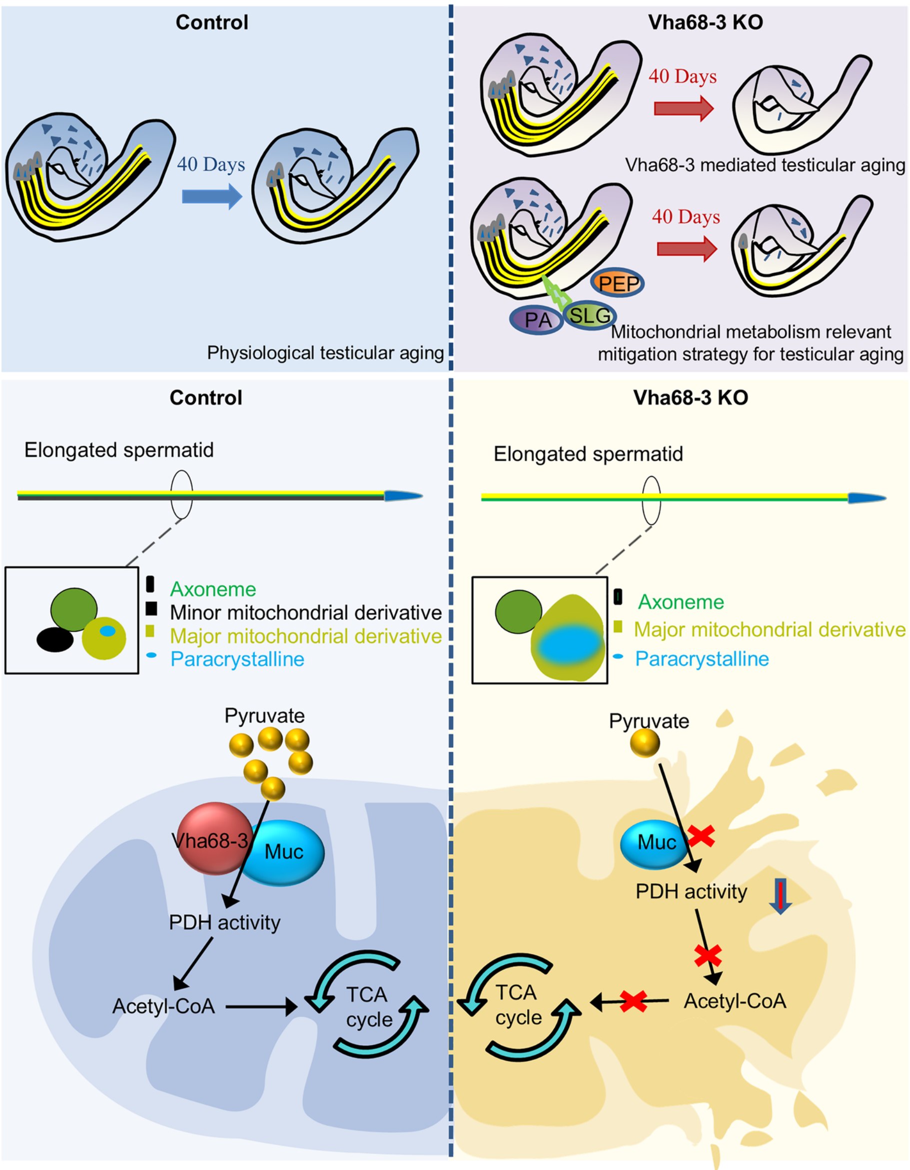

Fig. 10 The schematic diagram and improvement strategy of Vha68-3 in regulating testicular aging

paracrystalline structures [38, 39], which are primarily composed of S-Lap proteins that directly regulate male fertility [39]. A recent study further indicates that ND-42, a component of the mitochondrial electron transport chain complex I, plays a pivotal role in maintaining the mitochondrial structures of elongated spermatids, offering insights into the mitochondrial regulatory network at single-cell resolution [13].

While lysosomes are integral to the acidification of early spermatogenic cells in *Drosophila* testes [40], the precise mechanism through which Vha68-3 influences spermiogenesis at the tail end of elongated spermatids remains elusive. It is as yet unclear whether this regulation is mediated by lysosomal acidification or a direct impact on mitochondrial function. Previous studies have reported the absence of lysosomal structures at the tail end of spermatids in nematodes and mammals [41]. Our investigation, utilizing transmission electron microscopy and Lyso-Tracker staining, similarly found no evidence of lysosomes at the tail end of elongated spermatids in *Drosophila* testes. These findings collectively suggest that Vha68-3 may regulate spermiogenesis by directly influencing mitochondrial function.

ATP synthase, the principal source of energy for cellular processes, plays a vital role in the maintenance and differentiation of testicular spermatogenic cells, as demonstrated in genome-wide screening studies [42, 43]. The work of Ruth Lehmann's team has also highlighted the supportive role of ATP synthase in mitochondrial maturation and germ cell differentiation [44]. Moreover, Knotted onions (Knon), a testis-specific ATP synthase, has been shown to localize predominantly on the mitochondria of elongated spermatids, where it is essential for mitochondrial derivative formation [45]. Thus, dysfunction in testis-specific ATP synthase may serve as a critical pathway for disruptions in mitochondrial maintenance in elongated spermatids, contributing to male infertility.

Testis-specific genes appear to have pivotal roles at specific stages of spermatogenesis. For instance, the *big bubble 8* (*bb8*) gene, when mutated, leads to mitochondrial enlargement and the formation of paracrystalline structures in both major and minor mitochondrial derivatives of elongated spermatids, ultimately causing male infertility [46]. Intriguingly, knockout of *Vha68-3*, encoding a testis-specific V-type ATP synthase, in *Drosophila* results in swelling and impairment of the major mitochondrial derivatives and a complete loss of the minor mitochondrial derivatives in elongated spermatids, leading to male reproductive disorders. Further investigation revealed that Vha68-3 interacts with Muc, a key protein in the mitochondrial PDH complex, and *Vha68-3* KO decreases PDH activity and PA levels. This evidence suggests that Vha68-3 may regulate mitochondrial metabolism to maintain mitochondrial functionality in elongated spermatids.

Research indicates that PA, a byproduct of energy metabolism, plays a significant role in sperm viability and male reproductive capacity [47]. PA is transported from the cytoplasm to the mitochondrial matrix, where it is converted into acetyl-CoA by the PDH complex, before entering the TCA cycle [48]. Muc, a crucial protein in the PDH complex, is known to regulate pyruvate metabolism [49]. However, the precise role of mitochondrial events, including pyruvate metabolism, in spermiogenesis remains underexplored.

To comprehensively elucidate the impact of *Vha68-3* deficiency on male reproductive capacity, spermiogenesis, and mitochondrial function, this study employed multi-omics approaches, including Vha68-3 binding proteins, single-cell transcriptomics, and nontargeted metabolomics profiling. The key findings of this research are: (1) Vha68-3 interacts with Muc, and its absence leads to disruptions in spermiogenesis and impaired mitochondrial derivatives; (2) nontargeted metabolomics and single-cell transcriptomics suggest the involvement of mitochondrial metabolic pathways, particularly pyruvate metabolism, in *Vha68-3* deficiency-mediated spermiogenesis disorders; (3) loss of *Vha68-3* results in decreased PDH activity and PA levels in testes. These findings suggest that Vha68-3 maintains mitochondrial homeostasis during spermiogenesis by forming a complex with Muc to regulate mitochondrial metabolism.

In line with our research theory, we explored dietary supplementation to elevate PA levels in testes. Remarkably, supplementing the diet with PA significantly alleviated *Vha68-3* deficiency-mediated testicular aging characteristics. Through transcriptome–metabolomics correlation analysis, we identified two other downregulated metabolites, SLG and PEP, in *Vha68-3*-deficient flies. Dietary supplementation of these compounds effectively mitigated mitochondrial dysfunctions in elongated spermatids associated with testicular aging. SLG can be converted into lactate and GSH via glyoxalase II [50, 51], with lactate further metabolized into PA by lactate dehydrogenase [52]. Additionally, pyruvate kinase catalyzes the final step of glycolysis, converting PEP to PA [53]. Exogenous supplementation of mitochondrial metabolism-associated metabolites at early stage could bypass the metabolic bottleneck caused by *Vha68-3* loss. This exogenous metabolic support mitigates the effects of *Vha68-3* deficiency, thereby rescuing spermiogenesis defects without altering the genetic KO status. These findings underscore the potential of targeting pyruvate metabolism through compound screening as a novel therapeutic approach for testicular aging.

Conclusions

Collectively, this study provides a comprehensive understanding of the role of Vha68-3 in regulating spermiogenesis and mitochondrial derivative homeostasis via pyruvate metabolism during testicular aging. Furthermore, the dietary supplementation of key mitochondrial metabolic compounds presents a promising strategy to mitigate mitochondrial damage in elongated spermatids, offering novel avenues for treating spermiogenesis disorders linked to testicular aging.

Abbreviations

PA	Pyruvate
SLG	*S*-lactoylglutathione
PEP	Phosphoenolpyruvate
CEP78	Centrosomal protein 78
CFAP57	Cilia and flagella associated protein 57
FXR1	FMR1 autosomal homolog 1
ATF4	Activating transcription factor 4
mTORC1	Mechanistic target of rapamycin complex 1
Vha68-3	V-type ATPase 68 kDa subunit 3
gRNA	Guide RNA
PFA	Paraformaldehyde
BSA	Bovine serum albumin
RT	Room temperature
TEM	Transmission electron microscopy
KLH	Keyhole Limpet Hemocyanin
FDR	False discovery rate
POS	Positive ion mode
NEG	Negative ion mode
PLS-DA	Partial least squares discriminant analysis
OSC	Orthogonal signal correction
SEM	Standard error of the mean
Muc	Midline uncoordinated
PDH	Pyruvate dehydrogenase
OPLS-DA	Orthogonal projection to latent structures-discriminant analysis
VIP	Variable importance in projection
Knon	Knotted onions
bb8	Big bubble 8

Supplementary Information

The online version contains supplementary material available at https://doi.org/10.1186/s11658-025-00737-3.

Additional file 1. Fig. S1. Analysis of *Vha68-3* expression patterns and generation of *Vha68-3* KO flies. Fig. S2. Quantification of elongated spermatids in control and Vha68-3 KO testes. Fig. S3. Testicular phenotype analysis after Vha68-3 deletion at 40 days. Fig. S4. Quantification of mitochondrial phenotypes in control and Vha68-3 KO testes. Fig. S5. Quality control of scRNA-seq in *Drosophila* testes. Fig. S6. Pseudotime trajectory analysis reveals novel stages in testicular germ cell populations. Fig. S7. DEGs analysis in novel stages of testicular germ cell populations. Fig. S8. Enrichment analysis for DEGs in the Spermatocytes_Spermatids cluster. Fig. S9. Enrichment analysis of Vha68-3 binding proteins. Fig. S10. Correlation heatmap of the top 100 metabolites mediated by *Vha68-3* deletion. Fig. S11. Examinations of mitochondrial metabolism related indicators in control and Vha68-3 KO groups at 2 days. Fig. S12. Transcriptome analysis mediated by *Vha68-3* deletion. Fig. S13. Transcriptome–metabolomics association analysis for key pathways. Fig. S14. Protein–molecular interaction analysis. Fig. S15. Rescue effects of SLG and PEP in mitigating *Vha68-3* deletion-induced spermiogenesis defects during testicular aging. Table S1. The average expression levels of marker genes in each cell cluster. Table S2. The abundantly expressed genes in each cellular cluster. Table S3. Identification of Vha68-3 binding proteins via LC-MS/MS. Table S4. Detailed residues for Vha68-3/Muc interactions. Table S5. Identification of differential metabolites between 40-day-old control and Vha68-3 KO groups via nontargeted metabolomics. Table S6. Identification of DEGs between 40-day-old control and Vha68-3 KO groups via transcriptome. Table S7. Detailed residues at the contact interfaces for the Vha68-3/PA interactions. Table S8. Detailed residues at the contact interfaces for the Vha68-3/SLG interactions. Table S9. Detailed residues at the contact interfaces for the Vha68-3/PEP interactions.

Acknowledgements

The authors wish to thank all study participants, research staff, and students who assisted with this work. We are grateful to Singleron Biotechnologies for scRNA-seq and Gene Denovo Biotechnology for transcriptome–metabolomics association study and assisting with bioinformatics analysis of scRNA-seq in this study.

Author contributions

J.Y., B.Z., and F.S. initiated the project, designed the study, coordinated the experiment, and wrote the manuscript. Q.H., Y.F., L.H., C.S., X.C., Z.L., J.L., C.W., X.W., B.Y., and Z.L. performed the experiments and provided conceptual inputs for the paper. C.Q., X.T., X.Y., H.C., and Y.Z. analyzed the data. All authors read and approved the final manuscript.

Funding

This work was supported by the National Natural Science Foundation of China (32470899, 82471641, 32470903, 82401874, U24A20657, 82371613, and 82271633), Natural Science Foundation of Jiangsu Province (BK20221376 and BK20241858), Key Research and Development Program of Zhejiang Province (2023C03035), Nantong Project of Science and Technology (MS12022027), Scientific Research Project of Gusu School of Nanjing Medical University (GSKY202410304), Suzhou Gu Su Health Talent Research Project (GSWS2023056), Basic Research Foundation of Zhenjiang (JC2024024), Medical Research Project of Jiangsu Provincial Health Commission (M2022071), and Qinglan Project of Jiangsu Province of China.

Availability of data and material

The raw scRNA-seq data reported in this paper have been deposited in the Genome Sequence Archive (Genomics, Proteomics & Bioinformatics 2021) in National Genomics Data Center (Nucleic Acids Res 2022), China National Center for Bioinformation/Beijing Institute of Genomics, Chinese Academy of Sciences (GSA: CRA011800 and CRA019151) that are publicly accessible at https://ngdc.cncb.ac.cn/gsa. The mass spectrometry proteomics data have been deposited to the ProteomeXchange Consortium via the PRIDE partner repository with the dataset identifier PXD060509.

Declarations

Ethics approval and consent to participate

Not involved.

Consent for publication

None.

Competing interests

The authors declare no competing interests.

Author details

[1]Institute of Reproductive Medicine, Medical School, Nantong University, Nantong 226001, China. [2]State Key Laboratory of Reproductive Medicine and Offspring Health, Center for Reproduction and Genetics, Suzhou Municipal Hospital, Gusu School, The Affiliated Suzhou Hospital of Nanjing Medical University, Nanjing Medical University, Suzhou 215002, China. [3]Center for Reproductive Medicine, Department of Obstetrics and Gynecology, Affiliated Hospital of Nantong University, Nantong 226001, China. [4]Department of Andrology, Nanjing Drum Tower Hospital, The Affiliated Hospital of Nanjing University Medical School, Nanjing 210008, China. [5]Department of Clinical Pharmacy, The Affiliated Hospital of Jiangsu University, Jiangsu University, Zhenjiang 212001, China. [6]Reproductive Medicine Center, The Affiliated Maternity and Child Health Care Hospital of Nantong University, Nantong 226001, China. [7]Department of Obstetrics and Gynecology, The Affiliated Hospital of Nantong University, Nantong University, Nantong 226001, China. [8]Guangzhou Women and Children's Medical Center, GMU-GIBH Joint School of Life Science, The Guangdong-Hong Kong-Macao Joint

Laboratory for Cell Fate Regulation and Diseases, Guangzhou Medical University, Guangzhou 511495, China. [9]Department of Histology and Embryology, School of Medicine, Yangzhou University, Yangzhou 225009, China. [10]School of Basic Medical Sciences, Key Laboratory of Fertility Preservation and Maintenance of Ministry of Education, Ningxia Medical University, Yinchuan 750004, China.

Received: 10 December 2024 Accepted: 23 April 2025

References

1. Huang Q, Chen X, Yu H, Ji L, Shi Y, Cheng X, et al. Structure and molecular basis of spermatid elongation in the *Drosophila* testis. Open Biol. 2023;13(11): 230136.
2. Chebbo S, Josway S, Belote JM, Manier MK. A putative novel role for Eip74EF in male reproduction in promoting sperm elongation at the cost of male fecundity. J Exp Zool B Mol Dev Evol. 2021;336(8):620–8.
3. Gilmutdinov R, Kozlov EN, Yakovlev KV, Olenina LV, Kotov AA, Barr J, et al. The 3'UTR of the *Drosophila* CPEB translation factor gene orb2 plays a crucial role in spermatogenesis. Development. 2021;148(17):198788.
4. Shimada K, Park S, Miyata H, Yu Z, Morohoshi A, Oura S, et al. ARMC12 regulates spatiotemporal mitochondrial dynamics during spermiogenesis and is required for male fertility. Proc Natl Acad Sci U S A. 2021;118(6): e2018355118.
5. Bauerly E, Akiyama T, Staber C, Yi K, Gibson MC. Impact of cilia-related genes on mitochondrial dynamics during *Drosophila* spermatogenesis. Dev Biol. 2022;482:17–27.
6. Ma A, Zhou J, Ali H, Abbas T, Ali I, Muhammad Z, et al. Loss-of-function mutations in CFAP57 cause multiple morphological abnormalities of the flagella in humans and mice. JCI Insight. 2023;8(3): e166869.
7. Zhu T, Zhang Y, Sheng X, Zhang X, Chen Y, Zhu H, et al. Absence of CEP78 causes photoreceptor and sperm flagella impairments in mice and a human individual. Elife. 2023;12: e76157.
8. Kang J-Y, Wen Z, Pan D, Zhang Y, Li Q, Zhong A, et al. LLPS of FXR1 drives spermiogenesis by activating translation of stored mRNAs. Science. 2022;377(6607):6647.
9. Cong J, Yang Y, Wang X, Shen Y, Qi H-T, Liu C, et al. Deficiency of X-linked TENT5D causes male infertility by disrupting the mRNA stability during spermatogenesis. Cell Discov. 2022;8(1):23.
10. Dil S, Khan A, Unar A, Yang M-L, Ali I, Zeb A, et al. A novel homozygous frameshift variant in DNAH8 causes multiple morphological abnormalities of the sperm flagella in a consanguineous Pakistani family. Asian J Androl. 2023;25(3):350–5.
11. Lv M, Tang D, Yu H, Geng H, Zhou Y, Shao Z, et al. Novel FSIP2 variants induce super-length mitochondrial sheath and Asthenoteratozoospermia in humans. Int J Biol Sci. 2023;19(2):393–411.
12. Deng H, Dodson MW, Huang H, Guo M. The Parkinson's disease genes pink1 and parkin promote mitochondrial fission and/or inhibit fusion in *Drosophila*. Proc Natl Acad Sci U S A. 2008;105(38):14503–8.
13. Yu J, Li Z, Fu Y, Sun F, Chen X, Huang Q, et al. Single-cell RNA-sequencing reveals the transcriptional landscape of ND-42 mediated spermatid elongation via mitochondrial derivative maintenance in *Drosophila* testes. Redox Biol. 2023;62: 102671.
14. Cotter K, Stransky L, McGuire C, Forgac M. Recent Insights into the structure, regulation, and function of the V-ATPases. Trends Biochem Sci. 2015;40(10):611–22.
15. Eaton AF, Merkulova M, Brown D. The H+-ATPase (V-ATPase): from proton pump to signaling complex in health and disease. Am J Physiol Cell Physiol. 2021;320(3):C392–414.
16. Li TY, Wang Q, Gao AW, Li X, Sun Y, Mottis A, et al. Lysosomes mediate the mitochondrial UPR via mTORC1-dependent ATF4 phosphorylation. Cell Discov. 2023;9(1):92.
17. Dong S, Chen C, Zhang J, Gao Y, Zeng X, Zhang X. Testicular aging, male fertility and beyond. Front Endocrinol (Lausanne). 2022;13:1012119.
18. Deng Z, Zhao L, Li S, Chen X, Ling X, Zheng J, et al. Targeting dysregulated phago-/auto-lysosomes in Sertoli cells to ameliorate late-onset hypogonadism. Nat Aging. 2024;4(5):647–63.
19. Huang Q, Li J, Qi Y, He X, Shen C, Wang C, et al. Copper overload exacerbates testicular aging mediated by lncRNA:CR43306 deficiency through ferroptosis in *Drosophila*. Redox Biol. 2024;76: 103315.
20. Yu Z, Ren M, Wang Z, Zhang B, Rong YS, Jiao R, et al. Highly efficient genome modifications mediated by CRISPR/Cas9 in *Drosophila*. Genetics. 2013;195(1):289–91.
21. Liu W, Duan X, Fang X, Shang W, Tong C. Mitochondrial protein import regulates cytosolic protein homeostasis and neuronal integrity. Autophagy. 2018;14(8):1293–309.
22. Yu J, Wu H, Wen Y, Liu Y, Zhou T, Ni B, et al. Identification of seven genes essential for male fertility through a genome-wide association study of non-obstructive azoospermia and RNA in terference-mediated large-scale functional screening in *Drosophila*. Hum Mol Genet. 2015;24(5):1493–503.
23. Wang Y, Xu R, Cheng Y, Cao H, Wang Z, Zhu T, et al. RSBP15 interacts with and stabilizes dRSPH3 during sperm axoneme assembly in *Drosophila*. J Genet Genomics. 2019;46(6):281–90.
24. Szklarczyk D, Gable AL, Nastou KC, Lyon D, Kirsch R, Pyysalo S, et al. The STRING database in 2021: customizable protein-protein networks, and functional characterization of user-uploaded gene/measurement sets. Nucleic Acids Res. 2021;49(D1):D605–12.
25. Yu J, Fu Y, Li Z, Huang Q, Tang J, Sun C, et al. Single-cell RNA sequencing reveals cell landscape following antimony exposure during spermatogenesis in *Drosophila* testes. Cell Death Discov. 2023;9(1):86.
26. Zhang Z, Hu Y, Zheng X, Chen C, Zhao Y, Lin H, et al. Differential short-term and long-term metabolic and cytokine responses to infection of severe fever with thrombocytopenia syndrome virus. Metabolomics. 2024;20(4):84.
27. Li H, Janssens J, De Waegeneer M, Kolluru SS, Davie K, Gardeux V, et al. Fly Cell Atlas: a single-nucleus transcriptomic atlas of the adult fruit fly. Science. 2022;375(6584):2432.

28. Vasanthakumar T, Bueler SA, Wu D, Beilsten-Edmands V, Robinson CV, Rubinstein JL. Structural comparison of the vacuolar and Golgi V-ATPases from Sacc haromyces cerevisiae. Proc Natl Acad Sci U S A. 2019;116(15):7272–7.
29. Pu X, Qi B. Lysosomal dysfunction by inactivation of V-ATPase drives innate immune response in C. elegans. Cell Rep. 2024;43(5):114138.
30. Yang J, Anishchenko I, Park H, Peng Z, Ovchinnikov S, Baker D. Improved protein structure prediction using predicted interresidue orientations. Proc Natl Acad Sci U S A. 2020;117(3):1496–503.
31. Weng G, Wang E, Wang Z, Liu H, Zhu F, Li D, et al. HawkDock: a web server to predict and analyze the protein-protein complex based on computational docking and MM/GBSA. Nucleic Acids Res. 2019;47(W1):W322–30.
32. Liu Y, Yang X, Gan J, Chen S, Xiao Z-X, Cao Y. CB-Dock2: improved protein-ligand blind docking by integrating cavity detection, docking and homologous template fitting. Nucleic Acids Res. 2022;50(W1):W159–64.
33. Schoemans R, Aigrot M-S, Wu C, Marée R, Hong P, Belachew S, et al. Oligodendrocyte development and myelinogenesis are not impaired by high concentrations of phenylalanine or its metabolites. J Inherit Metab Dis. 2010;33(2):113–20.
34. Dobrowolski SF, Phua YL, Vockley J, Goetzman E, Blair HC. Phenylketonuria oxidative stress and energy dysregulation: emerging pathophysiological elements provide interventional opportunity. Mol Genet Metab. 2022;136(2):111–7.
35. Aging Biomarker C, Bao H, Cao J, Chen M, Chen M, Chen W, et al. Biomarkers of aging. Sci China Life Sci. 2023;66(5):893–1066.
36. López-Otín C, Blasco MA, Partridge L, Serrano M, Kroemer G. Hallmarks of aging: an expanding universe. Cell. 2023;186(2):243–78.
37. Zhang Z, Miao J, Wang Y. Mitochondrial regulation in spermatogenesis. Reproduction. 2022;163(4):R55–69.
38. Fabian L, Brill JA. *Drosophila* spermiogenesis: big things come from little packages. Spermatogenesis. 2012;2(3):197–212.
39. Laurinyecz B, Vedelek V, Kovács AL, Szilasi K, Lipinszki Z, Slezák C, et al. Sperm-Leucylaminopeptidases are required for male fertility as structural components of mitochondrial paracrystalline material in *Drosophila* melanogaster sperm. PLoS Genet. 2019;15(2): e1007987.
40. Zohar-Fux M, Ben-Hamo-Arad A, Arad T, Volin M, Shklyar B, Hakim-Mishnaevski K, et al. The phagocytic cyst cells in *Drosophila* testis eliminate germ cell progenitors via phagoptosis. Sci Adv. 2022;8(24):4937.
41. Liu P, Shi J, Sheng D, Lu W, Guo J, Gao L, et al. Mitopherogenesis, a form of mitochondria-specific ectocytosis, regulates sperm mitochondrial quantity and fertility. Nat Cell Biol. 2023;25(11):1625–36.
42. Tamirisa S, Papagiannouli F, Rempel E, Ermakova O, Trost N, Zhou J, et al. Decoding the regulatory logic of the drosophila male stem cell system. Cell Rep. 2018;24(11):3072–86.
43. Staehr C, Aalkjaer C, Matchkov VV. The vascular Na, K-ATPase: clinical implications in stroke, migraine, and hypertension. Clin Sci (Lond). 2023;137(20):1595–618.
44. Teixeira FK, Sanchez CG, Hurd TR, Seifert JRK, Czech B, Preall JB, et al. ATP synthase promotes germ cell differentiation independent of oxidative phosphorylation. Nat Cell Biol. 2015;17(5):689–96.
45. Sawyer EM, Brunner EC, Hwang Y, Ivey LE, Brown O, Bannon M, et al. Testis-specific ATP synthase peripheral stalk subunits required for tissue-specific mitochondrial morphogenesis in *Drosophila*. BMC Cell Biol. 2017;18(1):16.
46. Vedelek V, Laurinyecz B, Kovács AL, Juhász G, Sinka R. Testis-specific Bb8 Is essential in the development of spermatid mitochondria. PLoS ONE. 2016;11(8): e0161289.
47. Qian G-Q, Wang X-C, Zhang X, Shen B, Liu Q. Pyruvate kinase M in germ cells is essential for sperm motility and male fertility but not spermatogenesis. Asian J Androl. 2024;26(2):212–9.
48. Schell JC, Wisidagama DR, Bensard C, Zhao H, Wei P, Tanner J, et al. Control of intestinal stem cell function and proliferation by mitochondrial pyruvate metabolism. Nat Cell Biol. 2017;19(9):1027–36.
49. Zhu S, Niu Y, Zhou W, Liu Y, Liu J, Liu X, et al. Mitochondrial copper overload promotes renal fibrosis via inhibiting pyruvate dehydrogenase activity. Cell Mol Life Sci. 2024;81(1):340.
50. Jia X, Hollung K, Therkildsen M, Hildrum KI, Bendixen E. Proteome analysis of early post-mortem changes in two bovine muscle types: M. longissimus dorsi and M. semitendinosis. Proteomics. 2006;6(3):936–44.
51. Takagi D, Inoue H, Odawara M, Shimakawa G, Miyake C. The Calvin cycle inevitably produces sugar-derived reactive carbonyl methylglyoxal during photosynthesis: a potential cause of plant diabetes. Plant Cell Physiol. 2014;55(2):333–40.
52. Moens F, Lefeber T, De Vuyst L. Oxidation of metabolites highlights the microbial interactions and role of Acetobacter pasteurianus during cocoa bean fermentation. Appl Environ Microbiol. 2014;80(6):1848–57.
53. Lai T, Sun Y, Liu Y, Li R, Chen Y, Zhou T. Cinnamon oil inhibits *Penicillium expansum* growth by disturbing the carbohydrate metabolic process. J Fungi (Basel). 2021;7(2):123.

Publisher's Note